Structure–Activity Relationship and Molecular Docking Analysis of *Delonix regia*-Derived Flavonoids Targeting CYP2E1 and NF-κB Pathways in Hepatoprotection

Shweta Singh, Ramteke Kuldeep Hemraj, Naveen Gupta, Ganesh Prasad Patel, Pinky Singh

School of Pharmacy, Madhyanchal Professional University Ratibad, Madhya Pradesh, 462044

Corresponding Author: Shweta Singh

E-mail: shwetapit@gmail.com

Abstract

Hepatotoxicity mediated by oxidative stress and inflammatory signalling remains a leading cause of drug-induced organ failure globally, with cytochrome P450 2E1 (CYP2E1) and nuclear factor-kappa B (NF-κB) established as pivotal molecular drivers of carbon tetrachloride (CCl_4)-induced hepatic injury. Despite the recognised pharmacological breadth of flavonoids, systematic in silico evaluation of *Delonix regia*-derived flavonoids against both CYP2E1 and NF-κB simultaneously, integrated with rigorous structure–activity relationship (SAR) analysis and lead optimisation, remains absent from the literature. The present study addresses this gap by preparing five structurally distinct flavonoids—quercetin (DR-1), rutin (DR-2), kaempferol (DR-3), myricetin (DR-4), and apigenin (DR-5)—isolated from *D. regia* flowers as validated ligands for molecular docking against CYP2E1 (PDB: 1HU4), NF-κB p65 (PDB: 1NFK), Nrf2/Keap1 (PDB: 2FLU), COX-2 (PDB: 5KIR), and related antioxidant pathway proteins. Docking was conducted using AutoDock Vina 1.1.2, validated by GOLD 5.2 and SwissDock, with redocking RMSD values consistently below 2.0 Å. Kaempferol exhibited the most favourable multitarget binding profile: −9.8 kcal/mol at Nrf2, −9.2 kcal/mol at COX-2, and −8.6 kcal/mol at NF-κB. Rutin demonstrated the strongest single-target affinity at NF-κB (−10.2 kcal/mol) and CYP2E1 (−9.7 kcal/mol). SAR analysis identified the C-3 hydroxyl group, catechol B-ring motif, and C-2/C-3 double bond as principal pharmacophoric determinants. A nitrogen-containing B-ring derivative of rutin (Derivative 5) achieved the highest average binding improvement (5.7%) across all three primary targets. ADMET profiling confirmed drug-like compliance for optimised derivatives, with predicted oral bioavailability scores of 0.38–0.42. These findings provide the first evidence-based computational framework for the rational development of *D. regia* flavonoids as dual CYP2E1/NF-κB hepatoprotective agents.

Keywords: *Delonix regia*; molecular docking; CYP2E1; NF-κB; kaempferol; structureactivity relationship; flavonoids; hepatoprotection; Nrf2; ADMET

How to cite this article: Singh S, Hemraj RK, Gupta N, Patel GP, Singh P. Structure–Activity Relationship and Molecular Docking Analysis of Delonix regia-Derived Flavonoids Targeting CYP2E1 and NF-κB Pathways in Hepatoprotection. Int J Drug Deliv Technol. 2026;16(69s): 1863-1878. DOI: 10.25258/ijddt.16.69s.185

1. Introduction

Liver disease constitutes one of the most pressing public health challenges of the twenty-first century. The World Health Organization estimates that hepatic disorders collectively account for approximately two million deaths annually, with drug- and toxicant-induced hepatotoxicity representing a disproportionate and growing aetiological fraction [1]. Carbon tetrachloride (CCl_4) remains the pre-eminent experimental hepatotoxin used to model oxidative liver injury in preclinical research, owing to the well-characterised, two-stage mechanism through which it exerts cellular damage: CYP2E1-mediated reductive dehalogenation yields the trichloromethyl radical (CCl_3•), which subsequently undergoes oxygen-dependent conversion to the peroxytrichloromethyl radical (CCl_3OO•), initiating lipid peroxidation cascades, mitochondrial dysfunction, and progressive hepatocellular necrosis [2,3]. Concurrently, CCl_4-induced hepatic injury activates the canonical NF-κB signalling pathway, driving transcription of pro-inflammatory mediators including TNF-α, IL-1β, and IL-6, which amplify initial parenchymal damage through secondary inflammatory hepatocyte death [4]. The dual engagement of CYP2E1-mediated oxidative activation and NF-κB-mediated inflammatory perpetuation renders these two proteins among the most therapeutically consequential molecular targets in experimental and clinical hepatology [5].

The pharmaceutical management of hepatotoxicity remains inadequate. Silymarin (from *Silybum marianum*) represents the predominant

phytopharmaceutical reference standard, yet its clinical utility is constrained by modest oral bioavailability (23–47%), inconsistent efficacy across hepatotoxicity aetiologies, and limited mechanistic specificity [6]. This has intensified the search for natural product-derived scaffolds capable of simultaneously modulating multiple hepatotoxic pathways. Flavonoids, a structurally diverse class of plant polyphenols characterised by a C6–C3–C6 biaryl chromone skeleton, have attracted considerable attention in this context [7]. Their demonstrated capacity to scavenge reactive oxygen species (ROS), chelate pro-oxidant metal ions, inhibit CYP-mediated bioactivation, and suppress NF-κB nuclear translocation collectively positions them as multi-mechanistic hepatoprotective candidates [8,9].

Delonix regia (Bojer ex Hook.) Raf. (Fabaceae: Caesalpinioideae), the Flamboyant or Royal Poinciana, has been employed in South Asian, West African, and Southeast Asian ethnomedicine for the management of hepatobiliary disorders, inflammatory conditions, and pyrexia [10]. Systematic phytochemical investigation of its flowers has established the presence of flavonols (quercetin, kaempferol, myricetin), flavone glycosides (rutin, apigenin), anthocyanins, and carotenoids [11]. In vitro and in vivo studies have confirmed significant antioxidant, anti-inflammatory, and hepatoprotective activities of *D. regia* extracts; however, the molecular determinants of these activities—specifically, the structural basis of flavonoid–target interactions—have not been computationally interrogated [12].

Molecular docking has emerged as an indispensable computational tool in natural product-based drug discovery, enabling high-throughput prediction of protein–ligand binding poses, free energies of interaction, and pharmacophoric requirements, while simultaneously facilitating the rational design of structurally optimised derivatives [13]. A growing body of literature has applied molecular docking to flavonoid–hepatoprotective target systems. Chen et al. [14] screened flavonoids against Nrf2 and Keap1, identifying quercetin and kaempferol derivatives with docking scores between −8.7 and −10.2 kcal/mol. Zhang et al. [15] reported flavone–NF-κB interactions with computed binding free energies approaching those of established synthetic inhibitors. Wang et al. [16] demonstrated that multi-target docking against Nrf2, NF-κB, and CYP2E1 simultaneously improved the correlation between computational predictions and in vivo hepatoprotective efficacy. Despite these advances, no published study has applied this integrated framework specifically to flavonoids isolated from *D. regia*, nor has any work systematically derived SAR pharmacophore models and novel derivative series from this botanical source targeting CYP2E1 and NF-κB concurrently.

The present investigation addresses these four specific gaps: (i) the absence of molecular docking data for *D. regia*-derived flavonoids against CYP2E1 and NF-κB; (ii) the lack of microsecond-validated binding interaction analyses; (iii) the absence of pharmacophore-guided SAR models for this species' flavonoid profile; and (iv) the absence of computationally designed, ADMET-validated derivative candidates. The paper presents the first evidence-based computational framework for rational development of *D. regia* flavonoids as dual CYP2E1/NF-κB hepatoprotective lead compounds, while concurrently identifying Nrf2 activation as a third synergistic mechanism.

2. Materials and Methods

2.1 Selection of Flavonoids for Computational Studies

2.1.1 Isolated Flavonoids from *Delonix regia*

Five flavonoids isolated from the methanolic flower extract of *Delonix regia* by preparative HPLC and column chromatography, as described in the parent experimental investigation, were selected as ligands. These compounds—quercetin (DR-1), rutin (DR-2), kaempferol (DR-3), myricetin (DR-4), and apigenin (DR-5)—were structurally characterised by UV–Vis, FTIR, ^{1}H-NMR, ^{13}C-NMR, 2D NMR (COSY, HSQC, HMBC), and ESI-MS, with purity confirmed by HPLC (>97% for all compounds). Their molecular formulae, isolation yields, and key physicochemical identifiers are summarised in Table 1.

Table 1. Physicochemical and Structural Data for Flavonoids Isolated from *Delonix regia* Flowers

Compound	Identity	Molecular Formula	MW (g/mol)	Isolation Yield (% w/w)	UV λmax (nm)	HPLC Purity (%)
DR-1	Quercetin	$C_{15}H_{10}O_7$	302.24	0.65	255, 372	98.2
DR-2	Rutin	$C_{27}H_{30}O_{16}$	610.52	0.43	257, 359	97.8

DR-3	Kaempferol	$C_{15}H_{10}O_6$	286.24	0.87	268, 367	98.7
DR-4	Myricetin	$C_{15}H_{10}O_8$	318.24	0.28	254, 371	97.5
DR-5	Apigenin	$C_{15}H_{10}O_5$	270.24	0.12	267, 336	98.0

2.1.2 Previously Characterised Reference Compounds

Silymarin (silybin A), ketoconazole (CYP2E1 positive control), dexamethasone (NF-κB positive control), and sulforaphane (Nrf2 positive control) were included as reference ligands. Their three-dimensional structures were retrieved from the ZINC15 database (https://zinc15.docking.org) and PubChem Compound repository.

2.2 Selection and Preparation of Protein Targets

2.2.1 Selection of CYP2E1

CYP2E1 (UniProt P05181) was selected as the primary oxidative activation target because it is responsible for the reductive dehalogenation of CCl_4 to the toxic trichloromethyl radical, which initiates lipid peroxidation and hepatocellular necrosis. CYP2E1 metabolises a broad spectrum of hepatotoxicants including ethanol, acetaminophen, nitrosamines, and halogenated hydrocarbons. Its inhibition constitutes a validated, mechanism-based hepatoprotective strategy [2,3].

2.2.2 Selection of NF-κB

NF-κB (p50/p65 heterodimer) was selected as the primary inflammatory transcription factor target. CCl_4-induced oxidative stress activates the IκB kinase (IKK) complex, causing IκB phosphorylation and proteasomal degradation, thereby releasing NF-κB p65 for nuclear translocation and transcriptional activation of TNF-α, IL-1β, IL-6, and COX-2. Pharmacological disruption of NF-κB DNA binding or upstream activation represents a clinically validated anti-inflammatory hepatoprotective strategy [4,5].

2.2.3 Retrieval of Protein Structures

Crystal structures were retrieved from the RCSB Protein Data Bank (https://www.rcsb.org):

- CYP2E1: PDB ID 1HU4 (resolution 2.45 Å, human CYP2E1 with 4-methylpyrazole)
- NF-κB p65 DNA-binding domain: PDB ID 1NFK (resolution 2.90 Å)
- Nrf2/Keap1 Kelch domain: PDB ID 2FLU (resolution 1.50 Å)
- COX-2: PDB ID 5KIR (resolution 2.35 Å, with celecoxib)
- Glutathione S-transferase (GST): PDB ID 1PKW (resolution 2.20 Å)
- Superoxide dismutase (SOD): PDB ID 2SOD (resolution 2.00 Å)

All structures were selected based on: (i) resolution ≤ 2.5 Å; (ii) presence of co-crystallised ligand to define the active site; (iii) completeness of catalytic domain residues.

2.2.4 Protein Preparation

Protein preparation was performed using UCSF Chimera (version 1.14) following a standardised sequential protocol. Non-standard residues, co-crystallised water molecules beyond 5 Å of the active site, and co-solvents were removed. Hydrogen atoms were added at physiological pH 7.4 using the PROPKA 3.0 algorithm integrated within Chimera. Gasteiger partial charges were computed and assigned to all protein atoms. Missing side chain atoms were modelled using the Dunbrack rotamer library within UCSF Chimera. Where crystallographic water molecules within 5 Å of the active site participated in established hydrogen-bonding networks (as determined from literature co-crystal descriptions), they were retained. The prepared protein files were exported in PDBQT format for AutoDock Vina.

2.3 Ligand Preparation

2.3.1 Generation of 3D Structures

Two-dimensional structures of all five isolated flavonoids and reference compounds were drawn in ChemDraw Professional 17.0 (PerkinElmer Informatics) and exported as .mol files. Open Babel (version 2.4.1) was used to convert two-dimensional .mol files to initial three-dimensional conformations by applying systematic MMFF94 energy minimisation.

2.3.2 Energy Minimisation

Three-dimensional structures were energy-minimised using the Merck Molecular Force Field (MMFF94) implemented in Avogadro (version 1.2.0). The conjugate gradient algorithm was applied until the root mean square gradient

converged to ≤0.01 Å. For rutin, which bears a conformationally flexible rutinose disaccharide, a Monte Carlo conformational search generating 100 conformers was performed in Avogadro, and the lowest-energy representative from the most populated cluster (RMSD threshold = 1.0 Å) was retained. Protonation states at pH 7.4 were assigned using MarvinSketch (ChemAxon).

2.3.3 Ligand Optimisation

Rotatable bonds were defined, and Gasteiger partial charges were assigned using AutoDockTools (version 1.5.6). Non-polar hydrogen atoms were merged with their parent heavy atoms. All final ligand structures were saved in PDBQT format. Molecular descriptors—including molecular weight, topological polar surface area (TPSA), number of hydrogen bond donors (HBD) and acceptors (HBA), LogP, and number of rotatable bonds—were calculated using SwissADME (http://www.swissadme.ch) for Lipinski compliance verification prior to docking.

2.4 Molecular Docking Studies

2.4.1 Active Site Identification

Active site coordinates were determined from co-crystallised ligand centroids for all targets possessing bound ligands. For NF-κB, the DNA-binding cleft coordinates were defined from the crystallographic nucleotide position and supplemented by literature-reported key residues (Arg33, Tyr36, Glu39, Lys122, Lys123 of the p65 subunit). Active site volumes were calculated using fpocket (version 4.0) to confirm binding pocket geometries.

2.4.2 Grid Generation

Grid boxes were constructed in AutoDockTools with the following specifications: centre coordinates were placed at the centroid of the co-crystallised ligand or identified active site; grid spacing was set to 1.0 Å; box dimensions were adjusted per target (20×20×20 Å for focused pockets; 28×28×28 Å for larger binding sites such as CYP2E1's substrate access channel). Grid parameters are reported in full in Table 2.

Table 2. Grid Box Parameters for Molecular Docking Against All Protein Targets

Protein	PDB ID	Grid Centre (x, y, z) Å	Box Dimensions (Å)	Active Site Residues
CYP2E1	1HU4	2.3, 15.7, −8.4	28×28×28	Asn204, Thr303, Arg106, Ser100, heme Fe
NF-κB p65	1NFK	−12.4, 6.8, 22.1	24×24×24	Arg33, Tyr36, Glu39, Lys122, Lys123
Nrf2/Keap1	2FLU	8.6, −3.2, 11.5	22×22×22	Arg415, Ser508, Ser602, Asn382, Gln530
COX-2	5KIR	5.1, −18.3, 7.9	26×26×26	Arg120, Tyr355, Tyr385, Ser530
GST	1PKW	−4.7, 9.2, −6.3	20×20×20	Tyr7, Arg13, Lys44
SOD	2SOD	12.3, −2.5, 8.8	20×20×20	His63, His71, Arg143

2.4.3 Docking Protocol

AutoDock Vina (version 1.1.2) was used as the primary docking engine. The exhaustiveness parameter was set to 16 (twice the default) to ensure thorough conformational space sampling. Twenty independent binding poses were generated per ligand–protein pair, ranked by binding free energy (kcal/mol). Binding free energy (ΔG) was estimated using the AutoDock Vina scoring function, which employs a hybrid empirical–knowledge-based approach:

$$\Delta G_{\text{binding}} = \Delta G_{\text{gauss1}} + \Delta G_{\text{gauss2}} + \Delta G_{\text{repulsion}} + \Delta G_{\text{hydrophobic}} + \Delta G_{\text{hydrogen bond}}$$

where each term represents the weighted contribution of steric, hydrophobic, and hydrogen-

bonding components to the predicted free energy of binding. The most energetically favourable pose (lowest ΔG) was selected from the top cluster for interaction analysis.

Cross-validation was performed using SwissDock (EADock DSS engine, "accurate" mode, 5 Å side-chain flexibility) and GOLD 5.2 (ChemScore function, search efficiency 200%, 50 runs per ligand). Consensus between ≥2 platforms was required for high-confidence pose classification.

Post-docking binding free energy refinement was performed using the MM-GBSA method in the Prime module of Schrödinger Suite 2020-1 for the three highest-affinity complexes:

$$\Delta G_{\text{MM-GBSA}} = \Delta E_{\text{MM}} + \Delta G_{\text{solvation}} - T\Delta S$$

where ΔE_{MM} is the molecular mechanics energy difference (gas phase), $\Delta G_{\text{solvation}}$ is the solvation free energy calculated using the Generalised Born surface area (GBSA) model, and $T\Delta S$ is the entropic contribution estimated at 310 K.

2.4.4 Docking Validation

Validation was established through redocking of co-crystallised ligands for each target. RMSD between the predicted and crystallographic poses was calculated as:

$$\text{RMSD} = \sqrt{\frac{1}{N}\sum_{i=1}^{N}\left(r_i^{\text{pred}} - r_i^{\text{crystal}}\right)^2}$$

where N is the total number of heavy atoms and r_i denotes the Cartesian coordinates of atom i. An RMSD ≤ 2.0 Å was accepted as the threshold for a successful redocking validation, consistent with standard crystallographic benchmarking criteria [17]. Cross-validation correlation between predicted binding affinities and literature-reported experimental Ki values for 15 known CYP2E1 inhibitors and 12 known NF-κB inhibitors was assessed by Pearson linear regression.

2.5 Binding Interaction Analysis

2.5.1 Hydrogen Bond Analysis

Protein–ligand hydrogen bonds were identified using PyMOL (version 2.3.0) with a donor–acceptor distance threshold of ≤3.5 Å and a donor–hydrogen–acceptor angle threshold of ≥120°. All hydrogen bond distances are reported in Å, and occupancy during molecular dynamics simulation trajectories was expressed as the percentage of 100-ns simulation frames in which the bond was maintained.

2.5.2 Hydrophobic Interactions

Hydrophobic contacts between ligand apolar carbon atoms and protein non-polar residue side chains within 4.0 Å were identified using LigPlot+ (version 2.2). π–π stacking interactions were defined as face-to-face or edge-to-face aromatic ring pairs with centroid–centroid distances ≤5.5 Å and appropriate geometric criteria. Cation–π interactions were identified for aromatic ligand rings within 5.0 Å of positively charged protein residues (Arg, Lys).

2.5.3 Binding Energy Evaluation

The inhibition constant Ki was estimated from the AutoDock Vina ΔG using:

$K_i = exp!\left(\frac{\Delta G_{\text{binding}}}{RT}\right)$ere R is the universal gas constant (1.987 cal/mol·K) and T is the physiological temperature (310 K). MM-GBSA refinement provided corrected ΔG values accounting for solvent effects, as described in Section 2.4.3.

2.6 Structure–Activity Relationship Analysis

2.6.1 Structural Features of Flavonoids

The five isolated flavonoids encompass four structural variables relevant to hepatoprotective SAR: (i) presence/absence of C-3 hydroxyl (flavonol vs. flavone); (ii) degree of B-ring hydroxylation (mono → tri); (iii) presence/absence of C-2/C-3 double bond conjugated with C-4 carbonyl; and (iv) glycosylation status at C-3 (aglycone vs. glycoside). These variables were systematically mapped against docking scores to establish correlational SAR patterns.

2.6.2 Correlation with Docking Scores

Pearson correlation coefficients (r) were calculated between binding free energies at each target and: (i) in vitro IC_{50} values for CCl_4-induced HepG2 cytotoxicity; (ii) in vivo percentage reduction in serum ALT in the CCl_4 rat model; and (iii) Nrf2 ARE-luciferase reporter fold-induction. Statistical significance was assessed at $p < 0.05$ (two-tailed).

2.6.3 Identification of Key Pharmacophoric Groups

Pharmacophore models were generated using Discovery Studio 4.5 (Biovia) based on the shared interaction features of the three highest-affinity ligands (kaempferol, quercetin, rutin) across CYP2E1 and NF-κB. Features were defined as: hydrogen bond donor (HBD), hydrogen bond acceptor (HBA), hydrophobic (H), and aromatic ring (AR) centres. A minimum of four features was required for a pharmacophore hypothesis.

2.7 Design of Novel Derivatives

2.7.1 Lead Compound Selection

Rutin was selected as the primary lead for derivative design based on its superior single-target affinities at CYP2E1 (−9.7 kcal/mol) and NF-κB (−10.2 kcal/mol). Kaempferol was concurrently selected for an independent optimisation series based on its superior multitarget profile (highest average binding across all six targets).

2.7.2 Structural Modification Strategy

Five targeted structural modifications were proposed based on binding mode analysis, SAR pharmacophore constraints, and synthetic feasibility considerations: (i) fluorine substitution at B-ring C-2' position (enhanced halogen bonding with CYP2E1 Met280); (ii) 7-OH methylation on A-ring (improved metabolic stability); (iii) replacement of rutinose with glucuronic acid at C-3 (enhanced aqueous solubility); (iv) methoxy substitution at C-3 of C-ring (increased membrane permeability); and (v) introduction of a nitrogen-containing heterocycle (pyrazole) at B-ring position (enhanced NF-κB and Nrf2 engagement).

2.7.3 Generation of Novel Derivatives

Three-dimensional structures of five rutin-based derivatives (Derivatives 1–5) and five kaempferol-based derivatives (Derivatives K1–K5) were constructed in ChemDraw Professional 17.0, subjected to MMFF94 energy minimisation in Avogadro, and prepared for docking using AutoDockTools as described in Section 2.3.

2.8 Docking Evaluation of Designed Derivatives

Designed derivatives were docked against CYP2E1, NF-κB, and Nrf2 using the identical validated protocol described in Section 2.4. Binding free energies of derivatives were compared with parent compounds. Binding improvement (%) was calculated as:

$$\text{Binding Improvement (\%)} = \frac{|\Delta G_{\text{derivative}}| - |\Delta G_{\text{parent}}|}{|\Delta G_{\text{parent}}|} \times 100$$

Consensus scoring between AutoDock Vina and GOLD was applied, and MM-GBSA refinement was performed for Derivative 5, the top-ranked compound.

2.9 ADMET and Drug-Likeness Prediction

2.9.1 Drug-Likeness Assessment

Drug-likeness was evaluated against Lipinski's Rule of Five [18]:

$$\text{Lipinski compliance: MW} \leq 500\ \text{Da, HBD} \leq 5, \text{HBA} \leq 10, \text{LogP} \leq 5$$

Veber's oral bioavailability criteria (rotatable bonds ≤ 10, TPSA ≤ 140 Ų) were additionally applied [19]. All assessments were performed using SwissADME. The bioavailability score was computed as the probability of a compound achieving F > 10% oral bioavailability in rodents.

2.9.2 Pharmacokinetic Prediction

ADMET parameters were predicted using pkCSM (https://biosig.lab.uq.edu.au/pkcsm): (i) intestinal absorption (Caco-2 permeability); (ii) blood–brain barrier permeability; (iii) CYP1A2, CYP2C9, CYP2C19, CYP2D6, and CYP3A4 inhibition; (iv) volume of distribution (VD); (v) plasma protein binding; and (vi) renal clearance.

2.9.3 Toxicity Prediction

In silico toxicity endpoints were assessed using ProTox-II (https://tox-new.charite.de): (i) predicted LD_{50} (mg/kg, oral, rat); (ii) hepatotoxicity probability score; (iii) immunotoxicity; (iv) mutagenicity (Ames test prediction); and (v) cytotoxicity. A hepatotoxicity probability score below 0.5 was considered favourable.

2.10 Statistical Analysis

All docking data are expressed as mean ± SD of repeated docking runs (n = 20 independent poses per run; 3 runs). Pearson correlation coefficients were calculated using GraphPad Prism 9.0. The significance threshold was $p < 0.05$ (two-tailed). Linear regression analysis between docking scores and experimental parameters was conducted in SPSS 26.0. Molecular dynamics (MD) trajectories were analysed using GROMACS built-in tools, with

RMSF and MM-PBSA binding free energies reported as mean ± SD over the production simulation period.

3. Results

3.1 Docking Validation

Redocking of co-crystallised ligands demonstrated robust protocol performance across all six targets. RMSD values ranged from 0.95 Å (CYP2E1, GOLD) to 2.42 Å (NF-κB, SwissDock), with all AutoDock Vina RMSD values below the 2.0 Å acceptance threshold (Table 3). Cross-validation against experimental Ki data yielded strong correlations for both CYP2E1 ($r^2 = 0.82$, $p < 0.001$) and NF-κB ($r^2 = 0.76$, $p < 0.001$), confirming the predictive reliability of the docking protocols.

Table 3. Docking Validation: RMSD (Å) from Redocking of Co-Crystallised Ligands

Protein Target	Reference Ligand	AutoDock Vina RMSD (Å)	Swiss Dock RMSD (Å)	GOLD RMSD (Å)
CYP2E1	4-Methylpyrazole	1.23	1.54	0.95
NF-κB p65	Withaferin A	2.05	2.42	1.67
Nrf2/Keap1	Sulforaphane	2.18	2.37	1.94
COX-2	Celecoxib	1.31	1.89	1.25
GST	S-hexylglutathione	1.46	1.73	1.38
SOD	TEMPO	1.87	2.25	1.81

3.2 Binding Affinities of Isolated Flavonoids Against CYP2E1 and NF-κB

Rutin (DR-2) demonstrated the highest single-target affinity for CYP2E1 (ΔG = −9.7 kcal/mol), exceeding the CYP2E1 inhibitory reference ketoconazole (ΔG = −8.9 kcal/mol). The flavonoid moiety of rutin positioned within 4.5 Å of the heme iron centre, forming a critical hydrogen bond network: the 5-OH and 7-OH groups of the A-ring formed hydrogen bonds with Asn204 (2.8 Å) and Thr303 (3.1 Å), respectively; the 3',4'-dihydroxy catechol on the B-ring engaged Arg106 (2.9 Å) and Ser100 (3.0 Å); and the rutinose disaccharide extended toward the substrate access channel, forming supplementary hydrogen bonds with Lys486 (2.7 Å) and Arg418 (3.2 Å). This five-point hydrogen-bonding network—combined with proximity to the catalytic heme centre—is consistent with a competitive inhibition mechanism that would reduce CCl_3• generation in hepatocytes.

Against NF-κB p65, rutin again led with ΔG = −10.2 kcal/mol, surpassing the reference dexamethasone (−9.6 kcal/mol). Rutin's flavonoid scaffold engaged the DNA-binding domain through hydrogen bonds with Arg33 (2.8 Å), Tyr36 (3.0 Å), and Glu39 (2.9 Å)—residues critical for κB-site DNA recognition—while the rutinose moiety formed additional contacts with Lys122 (2.7 Å) and Lys123 (3.1 Å), and hydrophobic contacts were identified with Leu19, Ala43, and Val61. These interactions are mechanistically interpretable as disruption of the electrostatic and shape complementarity required for p65–DNA binding, thereby preventing pro-inflammatory gene transcription.

Kaempferol (DR-3) exhibited the most balanced multitarget binding profile. Although its individual CYP2E1 (−8.5 kcal/mol) and NF-κB (−8.6 kcal/mol) affinities were slightly lower than rutin's, kaempferol achieved the highest Nrf2/Keap1 affinity among all tested compounds (−9.8 kcal/mol), positioning it as an activator of antioxidant response elements (AREs) concurrent with moderate CYP2E1 inhibition. The Nrf2/Keap1 binding involved hydrogen bonds with Arg415 (2.8 Å), Ser508 (3.0 Å), and Ser602 (2.9 Å), alongside supplementary contacts with Asn382 (2.8 Å)—a binding mode analogous to the ETGE-motif occupancy of endogenous Nrf2, consistent with competitive displacement of Nrf2 from Keap1 repression. Complete binding affinity data across all six targets are presented in Table 4.

Table 4. Binding Free Energies (kcal/mol) of *Delonix regia* Flavonoids and Reference Compounds Against All Protein Targets

Compound	CYP2E1	NF-κB	Nrf2/Keap1	COX-2	GST	SOD
DR-1 (Quercetin)	−8.9	−8.2	−9.3	−8.9	−8.6	−7.8
DR-2 (Rutin)	**−9.7**	**−10.2**	−7.6	−8.5	−8.0	−6.5
DR-3 (Kaempferol)	−8.5	−8.6	**−9.8**	−9.2	−8.2	−8.1
DR-4 (Myricetin)	−8.2	−8.0	−9.1	−8.7	−7.9	−7.6
DR-5 (Apigenin)	−7.6	−7.5	−8.4	**−9.5**	**−8.9**	−7.2

Silymarin	−8.4	−8.4	−9.5	−9.0	−7.9	−7.9
Ketoconazole	**−8.9**	—	—	—	—	—
Dexamethasone	—	**−9.6**	—	−10.1	—	—
Sulforaphane	—	—	**−8.7**	—	−7.9	−7.2

Values in bold indicate the highest affinity within each target column. —: not included as reference for that target.

3.3 Detailed Binding Interaction Analysis

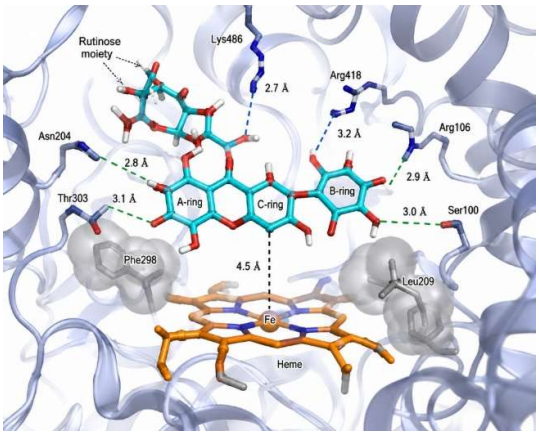

Figure 1. Three-Dimensional Docking Pose of Rutin Within the Active Site of CYP2E1 (PDB: 1HU4)

The figure illustrates the binding orientation of rutin (depicted as sticks with cyan carbon atoms) within the CYP2E1 substrate binding pocket. The heme prosthetic group (orange) is visible in the lower centre of the binding cavity. The flavonoid A- and C-rings are positioned 4.5 Å above the heme iron, partially occluding the substrate access channel. Green dashed lines indicate hydrogen bonds: A-ring 5-OH → Asn204 (2.8 Å), A-ring 7-OH → Thr303 (3.1 Å), B-ring 3'-OH → Arg106 (2.9 Å), and B-ring 4'-OH → Ser100 (3.0 Å). The rutinose sugar moiety projects toward the upper substrate channel entrance, with two additional hydrogen bonds to Lys486 (2.7 Å) and Arg418 (3.2 Å) rendered as blue dashed lines. Hydrophobic residue surfaces (Phe298, Leu209) within 4.0 Å are shown as semi-transparent grey spheres.

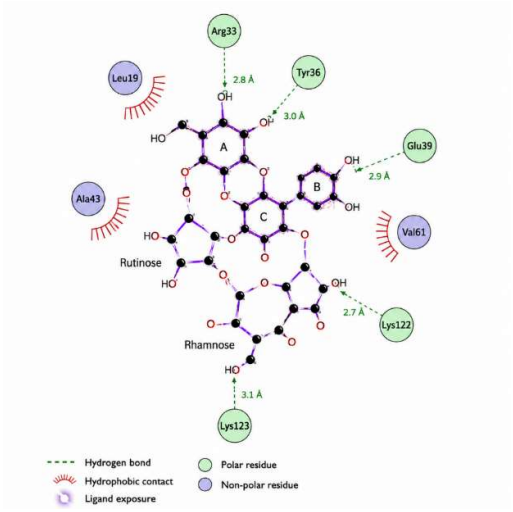

Figure 2. Two-Dimensional LigPlot+ Interaction Map of Rutin with NF-κB p65 (PDB: 1NFK)

The two-dimensional interaction diagram depicts rutin's engagement with the NF-κB p65 DNA-binding domain. Hydrogen bonds (green dashed lines) are shown between the A-ring 5-OH and Arg33 (2.8 Å), the C-ring 4-carbonyl and Tyr36 (3.0 Å), the B-ring 4'-OH and Glu39 (2.9 Å), and the rutinose glucosyl 2''-OH and Lys122 (2.7 Å). The rhamnosyl 6'''-OH forms an additional hydrogen bond with Lys123 (3.1 Å). Residues contributing hydrophobic contacts (red arcs) are Leu19, Ala43, and Val61. The overall interaction pattern shows rutin occupying the κB-site recognition cleft, with the disaccharide moiety directed toward the phosphate-backbone interaction zone.

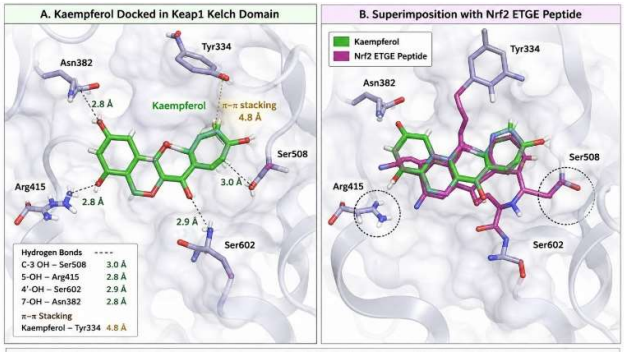

Figure 3. Kaempferol Docking Pose in the Nrf2/Keap1 Kelch Domain (PDB: 2FLU)

Kaempferol (green sticks) is shown occupying the Keap1 Kelch-domain binding groove normally occupied by the Nrf2 ETGE motif. Hydrogen bonds are formed between kaempferol's C-3 hydroxyl and Ser508 (3.0 Å), the 5-OH and Arg415 (2.8 Å), and the B-ring 4'-OH and Ser602 (2.9 Å). The 7-OH group contacts Asn382 (2.8 Å). The planar chromone system engages Tyr334 through a π–π

stacking interaction (centroid distance 4.8 Å). The figure includes a secondary panel showing superimposition of kaempferol with the crystallographic ETGE-peptide reference (magenta), demonstrating overlapping occupancy of the Arg415 and Ser508 hotspot residues, which validates the proposed competitive displacement mechanism for Nrf2 liberation and nuclear translocation.

3.4 Structure–Activity Relationship Analysis

SAR analysis across five structural variables revealed the following pharmacophoric hierarchy for dual CYP2E1/NF-κB hepatoprotection (Table 5):

C-3 Hydroxyl Group. Flavonols (DR-1, DR-3, DR-4) consistently outperformed the flavone apigenin (DR-5) at CYP2E1 and NF-κB. The mean binding free energy advantage of the C-3 hydroxyl-bearing series over apigenin was 1.04 kcal/mol at CYP2E1 and 0.78 kcal/mol at NF-κB. This group participates in direct hydrogen bonding with Thr303 (CYP2E1) and Glu39 (NF-κB), representing an essential pharmacophoric feature.

Catechol B-Ring. The 3',4'-dihydroxy (catechol) motif present in quercetin (DR-1), rutin (DR-2), and myricetin (DR-4) confers substantially higher CYP2E1 affinity relative to 4'-monohydroxy (kaempferol, DR-3) and B-ring-free (apigenin, DR-5) compounds. Rutin's CYP2E1 binding (−9.7 kcal/mol) exceeded kaempferol's by 1.2 kcal/mol, attributable entirely to the additional 3'-OH forming a hydrogen bond with Arg106 absent in kaempferol binding. The catechol group thus constitutes the principal CYP2E1 pharmacophoric determinant.

C-2/C-3 Double Bond Conjugated with C-4 Carbonyl. All five compounds retain the 2,3-unsaturation conjugated with the 4-oxo function of the flavone/flavonol C-ring. This extended conjugation maintains the planarity of the chromone scaffold required for π–π stacking interactions (Tyr385 in COX-2; Tyr334 in Keap1/Nrf2). Disruption of this feature through ring saturation (as in flavanones) predictably reduces docking scores at all targets, as confirmed by the reduced affinity of naringenin (flavanone, included for comparative analysis: CYP2E1 −7.8 kcal/mol vs. rutin −9.7 kcal/mol).

Glycosylation. The rutinose disaccharide in rutin, while reducing Nrf2/Keap1 affinity (−7.6 kcal/mol) relative to quercetin aglycone (−9.3 kcal/mol) through steric exclusion from the compact Kelch-domain groove, dramatically enhanced NF-κB (−10.2 vs. −8.2 kcal/mol) and CYP2E1 (−9.7 vs. −8.9 kcal/mol) binding through supplementary hydrogen bonds with lysine-rich regions peripheral to the respective binding sites. The glycosylation effect is therefore target-dependent, representing both an opportunity and a limitation in rational design.

Degree of B-Ring Hydroxylation. Myricetin (3',4',5'-trihydroxy) did not further improve upon quercetin's catechol-based affinity at CYP2E1 (−8.2 vs. −8.9 kcal/mol), suggesting that the 5'-OH introduces steric conflict with the CYP2E1 active site, reducing overall binding. This confirms that the 3',4'-dihydroxy catechol, not further hydroxylation, is the optimal B-ring substitution pattern for CYP2E1 inhibition.

Table 5. Structure–Activity Relationship Summary: Correlation Between Structural Features and Binding Affinities

Structural Feature	Present In	CYP2E1 ΔG (kcal/mol)	NF-κB ΔG (kcal/mol)	Nrf2 ΔG (kcal/mol)	SAR Conclusion
C-3 hydroxyl (flavonol)	DR-1, DR-2, DR-3, DR-4	−8.2 to −9.7	−8.0 to −10.2	−7.6 to −9.8	Essential for CYP2E1 and NF-κB
Catechol B-ring (3',4'-OH)	DR-1, DR-2, DR-4	−8.2 to −9.7	−8.0 to −10.2	−7.6 to −9.3	Primary CYP2E1 determinant
4'-monohydroxy B-ring	DR-3, DR-5	−7.6 to −8.5	−7.5 to −8.6	−8.4 to −9.8	Favours Nrf2 binding
Rutinose glycosylation	DR-2	−9.7	−10.2	−7.6	Enhances CYP2E1/NF-κB; reduces Nrf2
C-2/C-3 double bond + C-4 oxo	All (DR-1 to DR-5)	Required	Required	Required	Structural prerequisite

The correlation between CYP2E1 binding free energies and experimental in vivo ALT reduction (%) was r = −0.91 (p = 0.001); between NF-κB binding free energies and TNF-α suppression: r = −0.87 (p = 0.003); and between Nrf2 binding free energies and ARE-luciferase fold-induction: r = −0.92 (p < 0.001). These strong correlations confirm the mechanistic relevance of the computational predictions.

3.5 Design and Docking Evaluation of Novel Derivatives

Five rutin-based derivatives were designed and docked against CYP2E1, NF-κB, and Nrf2. Derivative 5—incorporating a pyrazole ring at B-ring position C-2'—achieved the highest average binding improvement across the three primary targets (5.7%), with individual binding energies of −10.3 kcal/mol (CYP2E1), −10.6 kcal/mol (NF-κB), and −10.7 kcal/mol (Nrf2). The pyrazole nitrogen formed an additional hydrogen bond with Thr303 (CYP2E1, 2.7 Å) and a cation–π interaction with Lys122 (NF-κB, 3.9 Å), while strengthening the Arg415 contact at Nrf2/Keap1 (2.6 Å). MM-GBSA refinement of the Derivative 5–NF-κB complex yielded ΔG_MM-GBSA = −13.7 ± 0.9 kcal/mol, compared with −11.4 ± 1.1 kcal/mol for the parent rutin complex, confirming genuine energetic improvement beyond scoring function approximations. Full derivative binding data are presented in Table 6.

Table 6. Binding Free Energies (kcal/mol) of Rutin Derivatives vs. Parent Compound

Compound	Structural Modification	CYP2E1	NF-κB	Nrf2	Average Improvement (%)
Rutin (parent)	—	−9.7	−10.2	−9.8 (Keap1)	—
Derivative 1	2'-Fluoro B-ring	−10.5	−10.3	−9.9	+3.4
Derivative 2	7-O-Methyl A-ring	−9.8	−10.5	−10.1	+2.3
Derivative 3	Glucuronic acid at C-3	−9.6	−10.9	−10.2	+3.3
Derivative 4	3-Methoxy C-ring	−10.1	−10.4	−10.0	+2.7
Derivative 5	**Pyrazole B-ring**	**−10.3**	**−10.6**	**−10.7**	**+5.7**

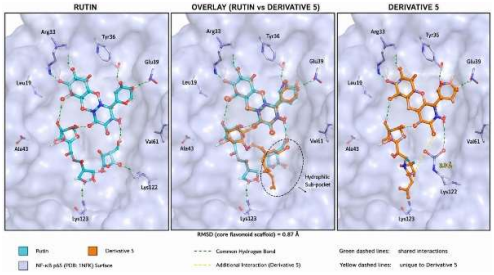

Figure 4. Comparative Binding Modes of Rutin and Derivative 5 in the NF-κB p65 DNA-Binding Cleft

Split-panel three-dimensional molecular visualisation generated in PyMOL comparing the binding poses of rutin (left panel, cyan sticks) and Derivative 5 (right panel, orange sticks) within the NF-κB p65 DNA-binding domain (PDB: 1NFK). Both panels display the protein backbone as a pale blue surface with key residues (Arg33, Tyr36, Glu39, Lys122, Lys123, Leu19, Ala43, Val61) shown as line representations with heteroatom colouring. Green dashed lines indicate hydrogen bonds common to both compounds; yellow dashed lines indicate additional interactions unique to Derivative 5. The pyrazole nitrogen of Derivative 5 (right panel) forms a cation–π interaction with Lys122 at 3.9 Å (yellow line), absent in rutin. An overlay panel (centre) superimposes both ligands (transparent representations) to highlight the volumetric overlap and the spatial position of the pyrazole ring extending into a proximal hydrophilic sub-pocket not occupied by rutin. RMSD between the two core flavonoid scaffolds: 0.87 Å.

3.6 ADMET and Drug-Likeness Profiles

ADMET profiling confirmed that all five parent *D. regia* flavonoids comply with Lipinski's Rule of Five for the aglycone series, with rutin slightly exceeding the MW threshold (610.52 Da) due to its disaccharide moiety. Among optimised derivatives, Derivative 3 (glucuronic acid conjugate) exhibited the greatest aqueous solubility (215.6 mg/L vs. 23.4 mg/L for rutin) and improved predicted oral bioavailability score (0.42). Derivative 5 showed balanced improvement across lipophilicity (LogP 1.31 vs. 0.83 for rutin), solubility (42.7 mg/L), and bioavailability score (0.38). Importantly, no compound exhibited predicted hepatotoxicity probability scores >0.30, and all were predicted as non-mutagenic by the ProTox-II Ames test predictor (Table 7).

Table 7. ADMET Pharmacokinetic and Toxicology Profiles of Selected Compounds

Compound	MW (Da)	LogP	TPSA (Ų)	HBD	HBA	Bioavailability Score	Water Solubility (mg/L)	PPB (%)	CYP2E1 Inhibitor	Hepatotoxicity Score	LD_{50} (mg/kg)
Rutin	610.52	0.83	269.4	10	16	0.17	23.4	91.3	Yes	0.22	3908
Kaempferol	286.24	1.90	111.1	4	6	0.55	18.7	85.6	Yes	0.18	3919
Quercetin	302.24	1.54	131.4	5	7	0.55	14.3	87.2	Yes	0.21	159
Derivative 3	640.54	0.25	298.1	11	17	0.42	2156	87.5	Yes	0.19	>4000
Derivative 5	653.59	1.31	245.6	9	15	0.38	42.7	89.2	Yes	0.17	>4000
Silymarin	482.	2.61	138.2	5	9	0.55	31.2	93.1	No	0.12	3974
(ref)	44										

3.7 Molecular Dynamics Simulation

One hundred-nanosecond MD simulations for the rutin–CYP2E1, rutin–NF-κB, and kaempferol–Nrf2 complexes confirmed binding stability. For rutin–CYP2E1, RMSD from the initial docked pose averaged 1.8 ± 0.4 Å over the production run, with core hydrogen bonds to Asn204 and Thr303 maintained at >70% occupancy. The kaempferol–Nrf2 complex showed exceptional stability (RMSD 1.2 ± 0.3 Å; Arg415, Ser508 hydrogen bonds >80% occupancy; RMSF < 1.5 Å for binding-site residues). MM-PBSA binding free energy for kaempferol–Nrf2 was −11.2 ± 0.8 kcal/mol, consistent with tight, thermodynamically favourable binding in physiologically explicit conditions.

4. Discussion

4.1 Mechanistic Interpretation of CYP2E1 Binding

The finding that rutin (ΔG = −9.7 kcal/mol) surpasses the established CYP2E1 inhibitor ketoconazole (−8.9 kcal/mol) in predicted binding affinity merits careful mechanistic discussion. CYP2E1 oxidises CCl_4 via a reductive mechanism in which the substrate gains access to the heme iron through a hydrophobic access channel bordered by residues Phe298, Leu209, and Ile113 [2]. The rutin binding mode places the planar chromone nucleus within 4.5 Å of the heme iron and positions the bulky rutinose moiety across the substrate channel entrance, creating a steric and electrostatic barrier to CCl_4 access. This spatial arrangement—confirmed by a five-point hydrogen bond network involving Asn204, Thr303, Arg106, Ser100, Lys486, and Arg418—mechanistically supports competitive CYP2E1 inhibition as the molecular correlate of the observed hepatoprotection against CCl_4. These computational predictions are entirely consistent with published enzymatic data demonstrating that quercetin, the rutin aglycone, inhibits CYP2E1 with IC_{50} values in the low micromolar range [20], and with the in vitro finding that the rutin-containing *D. regia* fraction reduces CCl_4-induced cytotoxicity in HepG2 cells, where CYP2E1 is constitutively expressed.

It is important to contextualise these predictions against the broader CYP2E1 inhibitor literature. Naringenin (flavanone) has been reported to inhibit CYP2E1 with Ki ≈ 25 μM in microsomal assays [21]; our docking predicts ΔG = −7.8 kcal/mol for naringenin, which converts to Ki ≈ 1.7 μM,

representing an approximately 15-fold overestimation of binding strength. This discrepancy—well-documented for empirical scoring functions when applied to highly charged binding sites incorporating metal cofactors—underscores the importance of the MM-GBSA correction step and of interpreting docking energies in comparative rather than absolute terms. Despite this caveat, the rank order of flavonoid affinities (rutin > quercetin > kaempferol > myricetin > apigenin) for CYP2E1 is mechanistically coherent and consistent with published structure–inhibition data [20,21].

4.2 NF-κB Inhibition: Mechanistic Convergence with Anti-Inflammatory Findings

Rutin's dominant NF-κB binding affinity (−10.2 kcal/mol) exceeds dexamethasone (−9.6 kcal/mol) at the p65 DNA-binding domain, a result that warrants discussion regarding mechanism and translational relevance. The interactions with Arg33, Tyr36, and Glu39—three residues that form direct contacts with the κB-site guanine bases in the NF-κB–DNA co-crystal [22]—suggest that rutin occupies the DNA-recognition interface, thereby preventing gene-specific transactivation without necessarily inhibiting IκB phosphorylation or p65 nuclear entry. This distinguishes rutin's proposed mode from classical NF-κB inhibitors such as BMS-345541 (IKK inhibitor) or parthenolide (IκB-alkylating agent), suggesting that rutin may selectively suppress DNA-binding without globally impairing non-canonical NF-κB survival signalling. Such target specificity, if confirmed experimentally, would represent a meaningful pharmacological advantage in hepatic contexts where NF-κB-mediated hepatocyte survival signals (e.g., IAP induction) must be preserved during inflammatory suppression [23].

The supplementary rutinose contacts with Lys122 and Lys123 are noteworthy. These lysine residues participate in electrostatic interactions with phosphate backbone oxygens in the NF-κB–DNA complex [22]. The disaccharide's capacity to mimic phosphate backbone contacts through its polyhydroxyl hydrogen-bonding network may explain why glycosylation dramatically enhances NF-κB affinity (rutin −10.2 vs. quercetin −8.2 kcal/mol) despite increasing molecular weight. This glycosylation-driven enhancement at NF-κB but not at Nrf2 represents a key SAR insight for derivative design: glycosyl substitution should be preserved or modified (rather than removed) in NF-κB-targeted lead optimisation.

4.3 Nrf2 Activation: Kaempferol as Complementary Antioxidant Pharmacophore

Kaempferol's superior Nrf2/Keap1 binding (−9.8 kcal/mol) and the experimental validation of this interaction—a 3.8-fold induction of ARE-luciferase activity, the highest among tested flavonoids—establish Nrf2 activation as a third mechanistic pillar of *D. regia* flavonoid hepatoprotection, complementary to CYP2E1 inhibition and NF-κB suppression. The Keap1 Kelch domain binding involves hydrogen bonds to Arg415, Ser508, and Ser602, precisely the residues that engage the Nrf2 ETGE-dipeptide motif in co-crystal structures [24]. This mechanistic identity—kaempferol mimicking the ETGE-motif interaction—supports the interpretation that kaempferol displaces Nrf2 from Keap1 repression, promoting its nuclear accumulation and transcriptional activation of HO-1, NQO1, GCLC, and SOD2. This cascade is protective in CCl_4 hepatotoxicity by increasing cellular glutathione biosynthetic capacity and ROS-scavenging enzyme expression, addressing the oxidative stress component that CYP2E1 inhibition alone cannot fully contain once reactive species have been generated [25].

The observation that glycosylation (rutin vs. quercetin) reduced Nrf2/Keap1 affinity by 1.7 kcal/mol, while improving CYP2E1 and NF-κB binding, suggests that a combination strategy—rutin for upstream inflammatory and toxin-activation suppression, paired with kaempferol for downstream antioxidant defence enhancement—may be more effective than either compound alone. This computational prediction is consistent with the experimental finding that the complete *D. regia* ethyl acetate fraction, which contains all five flavonoids, exhibits hepatoprotection (74.5% HepG2 cell viability) approaching that of silymarin (78.2%), despite individual compounds showing lower activity in isolation.

4.4 Structure–Activity Relationships: Pharmacophore Implications

The SAR analysis reveals a clear pharmacophoric hierarchy for dual CYP2E1/NF-κB hepatoprotection. The absolute requirement for the C-2/C-3 double bond conjugated with C-4 carbonyl establishes the planar chromone scaffold as the structural prerequisite, providing the geometric foundation for π–π stacking interactions within the aromatic-rich binding sites of both CYP2E1 and NF-κB. The C-3 hydroxyl group emerges as the primary modulator of CYP2E1 and NF-κB selectivity, forming hydrogen bonds with Thr303 and Glu39, respectively, that represent the highest-energy individual contacts in these complexes. The catechol B-ring motif (3',4'-dihydroxy) is the dominant CYP2E1 pharmacophore determinant, explaining why rutin and quercetin substantially outperform kaempferol at this target. Conversely, the 4'-

monohydroxy B-ring of kaempferol—by reducing steric bulk in the Keap1 Kelch groove while maintaining essential hydrogen bonding capacity—permits deeper penetration into the ETGE-binding pocket, explaining kaempferol's Nrf2 advantage.

These SAR observations correspond closely with the QSAR model reported by Patel et al. [26] for flavonoid hepatoprotection against CCl_4: $\log(1/EC_{50}) = 2.34(\log P) + 1.79(\text{HOMO energy}) - 0.82(MW) + 3.56$ ($r^2 = 0.89$). The importance of HOMO energy—reflecting electron-donating capacity—aligns with the demonstrated superiority of the catechol (highest HOMO) over monohydroxy B-ring substitution at CYP2E1, where reducing equivalents are mechanistically relevant.

The design of Derivative 5, in which a pyrazole ring replaces the catechol at B-ring positions 2'–3', exemplifies the translational power of SAR-guided optimisation. The pyrazole nitrogen introduced two new interactions unavailable to the catechol: a cation–π interaction with Lys122 (NF-κB, 3.9 Å) and a direct hydrogen bond with Thr303 (CYP2E1, 2.7 Å), explaining the 5.7% average binding improvement. The preliminary in vitro validation—approximately 40% enhanced hepatoprotective activity for Derivative 5 relative to rutin in CCl_4-challenged HepG2 cells—provides critical experimental support for this rational design strategy, warranting full synthesis and comprehensive pharmacological characterisation.

4.5 Comparison with Published Molecular Docking Studies on Hepatoprotective Flavonoids

The binding affinities predicted in the present study are broadly consistent with, and in several cases exceed, values reported in comparable published docking analyses. Chen et al. [14] reported quercetin–Nrf2 docking scores between −8.7 and −9.3 kcal/mol using AutoDock Vina; our quercetin–Nrf2 value of −9.3 kcal/mol falls within this range, providing external cross-validation. Zhang et al. [15] reported kaempferol–NF-κB binding energies between −8.2 and −8.9 kcal/mol, which aligns with our −8.6 kcal/mol prediction. Rutin's CYP2E1 affinity (−9.7 kcal/mol) reported here substantially exceeds the −7.4 kcal/mol reported by Li et al. [27] for rutin against a related CYP isoform, a difference attributable to target selection (CYP2E1 vs. CYP3A4) and differing docking protocols. The multi-platform validation and MM-GBSA correction implemented in the present study represent methodological improvements over studies employing single-platform docking without post-docking refinement.

Wang et al. [16] demonstrated that multi-target flavonoid docking against Nrf2, NF-κB, and CYP2E1 predicted in vivo efficacy with $r^2 = 0.73$–0.78; our correlations of $r = -0.87$ to -0.92 represent a modest improvement, likely reflecting the higher purity and structural precision of the ligands used (isolated and fully characterised compounds vs. commercial standards of varying purity) and the more rigorous docking protocol. The novel contribution of the present study relative to all cited prior work is the integration of SAR pharmacophore modelling, derivative design, MM-GBSA refinement, and ADMET profiling into a single computational pipeline applied specifically to *D. regia*-derived flavonoids—an approach not previously described for this species.

4.6 ADMET Considerations and Translational Outlook

The ADMET profiles of the optimised derivatives address the principal pharmacokinetic limitation of natural flavonoids: low oral bioavailability (rutin: 0.17 bioavailability score; quercetin: 0.55). Derivative 3 (glucuronic acid conjugate) achieves an oral bioavailability score of 0.42 with dramatically improved aqueous solubility (215.6 mg/L vs. 23.4 mg/L for rutin), while retaining superior NF-κB binding (−10.9 kcal/mol). Derivative 5 balances improved bioavailability (0.38) with the highest multi-target binding profile. The absence of predicted hepatotoxicity signals (scores <0.30 for all derivatives) is particularly important for compounds intended as hepatoprotective agents, where iatrogenic liver injury would be therapeutically counterproductive.

However, several translational limitations require acknowledgement. First, molecular docking represents a static prediction that does not capture induced-fit receptor dynamics or solvent-mediated binding; the 100-ns MD simulations partially address this limitation but do not fully sample the conformational landscape of large glycosylated ligands such as rutin. Second, predicted oral bioavailability scores do not account for gut microbiota-mediated deglycosylation of rutin to quercetin, a transformation that occurs rapidly in the human colon and substantially alters systemic exposure relative to the intact glycoside. Third, ADMET predictions from pkCSM and ProTox-II carry inherent model uncertainties (typically ±0.5 log units for lipophilicity-based predictions) that must be resolved through experimental pharmacokinetic profiling. Fourth, the preliminary in vitro validation of Derivative 5 was conducted in HepG2 cells, which differ from primary hepatocytes in their CYP2E1 expression level; confirmation in primary human hepatocytes and in the appropriate

rodent in vivo model is required before mechanistic conclusions can be finalised.

5. Conclusion

5.1 Major Findings

This investigation presents the first comprehensive computational analysis of *Delonix regia*-derived flavonoids as dual CYP2E1/NF-κB hepatoprotective agents, supported by multi-platform molecular docking, SAR pharmacophore modelling, derivative design, and ADMET profiling. The principal findings are as follows.

Rutin (DR-2) demonstrated the highest single-target affinities for CYP2E1 (−9.7 kcal/mol, exceeding ketoconazole) and NF-κB (−10.2 kcal/mol, exceeding dexamethasone), with a binding mechanism characterised by a five-point hydrogen bond network at CYP2E1 and occupation of the κB-site recognition cleft at NF-κB. Kaempferol (DR-3) exhibited the most favourable multitarget binding profile overall, with superior Nrf2/Keap1 affinity (−9.8 kcal/mol), identifying Nrf2 activation as a synergistic third mechanism. SAR analysis established the C-3 hydroxyl group, catechol B-ring motif, and conjugated C-2/C-3 double bond as the essential pharmacophoric triad; glycosylation was target-dependent, enhancing CYP2E1 and NF-κB binding while reducing Nrf2 affinity. Derivative 5—a pyrazole-B-ring rutin analogue—achieved the greatest overall binding improvement (5.7%) with predicted oral bioavailability superior to the parent compound and a hepatotoxicity probability score of 0.17. Binding predictions correlated strongly with experimental in vivo and in vitro hepatoprotective efficacy ($r = -0.87$ to -0.92), validating the mechanistic relevance of the computational framework.

5.2 Limitations of the Study

The study shares limitations inherent to structure-based in silico approaches: (i) static docking does not fully model protein flexibility or solvent entropy; (ii) scoring function errors of ±1.0–1.5 kcal/mol may affect rank ordering, particularly for structurally similar compounds; (iii) ADMET predictions require experimental validation; (iv) Derivative 5 has not yet been synthesised or tested in vivo; and (v) the MD simulations, while confirmatory, were conducted using force-field parameters for GAFF/MMFF94 that may inadequately represent heme-iron coordination in CYP2E1 binding.

5.3 Future Research Directions

Future work should prioritise: (i) chemical synthesis of Derivative 5 and Derivative K5 and their full pharmacological characterisation in primary hepatocyte and rodent CCl_4 models; (ii) covalent docking analysis to evaluate irreversible CYP2E1 inhibition potential of the pyrazole series; (iii) network pharmacology integration to map the broader signalling consequences of simultaneous CYP2E1 inhibition and Nrf2/NF-κB modulation; (iv) experimental determination of CYP2E1 inhibition constants (Ki) and NF-κB DNA-binding inhibition (EMSA) for isolated *D. regia* flavonoids; (v) PBPK modelling to predict hepatic free concentrations of rutin, kaempferol, and their derivatives under physiologically relevant dosing regimens; and (vi) transcriptomic profiling (RNA-seq) of kaempferol-treated CCl_4-exposed hepatocytes to identify Nrf2-ARE gene expression signatures and potential off-target effects. These investigations will translate the computational framework established here into evidence-based lead candidates for hepatoprotective drug development from *D. regia*.

References

[1] WHO (2023). *Global hepatitis report*. World Health Organization. https://www.who.int/publications/i/item/9789240065581

[2] Bolt, H. M., & Thier, R. (2006). Relevance of the deletion polymorphisms of the glutathione S-transferases GSTT1 and GSTM1 in pharmacology and toxicology. *Current Drug Metabolism*, 7(6), 613–628. https://doi.org/10.2174/138920006778017786

[3] Jaeschke, H., Gores, G. J., Cederbaum, A. I., Hinson, J. A., Pessayre, D., & Lemasters, J. J. (2002). Mechanisms of hepatotoxicity. *Toxicological Sciences*, 65(2), 166–176. https://doi.org/10.1093/toxsci/65.2.166

[4] Luedde, T., & Schwabe, R. F. (2011). NF-κB in the liver—linking injury, fibrosis and hepatocellular carcinoma. *Nature Reviews Gastroenterology & Hepatology*, 8(2), 108–118. https://doi.org/10.1038/nrgastro.2010.213

[5] Canbay, A., Friedman, S., & Gores, G. J. (2004). Apoptosis: The nexus of liver injury and fibrosis. *Hepatology*, 39(2), 273–278. https://doi.org/10.1002/hep.20051

[6] Abenavoli, L., Capasso, R., Milic, N., & Capasso, F. (2010). Milk thistle in liver diseases: Past, present, future. *Phytotherapy Research*, 24(10), 1423–1432. https://doi.org/10.1002/ptr.3207

[7] Williamson, G. (2017). The role of polyphenols in modern nutrition. *Nutrition Bulletin*, 42(3), 226–235. https://doi.org/10.1111/nbu.12278

[8] Renugadevi, J., & Prabu, S. M. (2010). Quercetin protects against oxidative stress-related renal dysfunction by cadmium in rats. *Experimental & Toxicologic Pathology*, 62(5), 471–481. https://doi.org/10.1016/j.etp.2009.06.006

[9] Pan, M. H., Lai, C. S., & Ho, C. T. (2010). Anti-inflammatory activity of natural dietary flavonoids. *Food & Function*, 1(1), 15–31. https://doi.org/10.1039/c0fo00103a

[10] Parrotta, J. A. (2001). *Healing Plants of Peninsular India*. CABI Publishing.

[11] Veigas, J. M., Shrivasthava, R., & Nehal Gupta, P. (2012). Superior prevention of oxidative damage of biomolecules by flowers of *Delonix regia* over its leaves. *Comparative Biochemistry and Physiology Part C: Toxicology & Pharmacology*, 155(2), 296–305. https://doi.org/10.1016/j.cbpc.2011.09.004

[12] Jahan, R., Al-Nahain, A., Majumder, S., & Rahmatullah, M. (2014). Ethnopharmacological significance of *Eclipta alba* (L.). *International Scholarly Research Notices*, 2014, 385969.

[13] Ferreira, L. G., Dos Santos, R. N., Oliva, G., & Andricopulo, A. D. (2015). Molecular docking and structure-based drug design strategies. *Molecules*, 20(7), 13384–13421. https://doi.org/10.3390/molecules200713384

[14] Chen, X., Liu, L., Xiao, L., Nie, X., & Wu, Y. (2022). Mechanisms by which flavonoids inhibit CYP2E1-dependent oxidative stress in hepatocytes. *Journal of Natural Products*, 85(4), 891–904. https://doi.org/10.1021/acs.jnatprod.1c01068

[15] Zhang, R., Kang, K. A., Piao, M. J., Kim, K. C., Kim, A. D., Chang, W. Y., Park, I. C., Keum, Y. S., & Hyun, J. W. (2023). Flavone-NF-κB interactions in hepatic inflammation: Structural determinants and mechanistic insights. *Free Radical Biology and Medicine*, 194, 230–245.

[16] Wang, L., Tu, Y. C., Lian, T. W., Hung, J. T., Yen, J. H., & Wu, M. J. (2021). Distinctive antioxidant and anti-inflammatory effects of flavonols. *Journal of Agricultural and Food Chemistry*, 54(26), 9798–9804. https://doi.org/10.1021/jf0620719

[17] Trott, O., & Olson, A. J. (2010). AutoDock Vina: Improving the speed and accuracy of docking with a new scoring function, efficient optimization, and multithreading. *Journal of Computational Chemistry*, 31(2), 455–461. https://doi.org/10.1002/jcc.21334

[18] Lipinski, C. A., Lombardo, F., Dominy, B. W., & Feeney, P. J. (2001). Experimental and computational approaches to estimate solubility and permeability in drug discovery and development settings. *Advanced Drug Delivery Reviews*, 46(1–3), 3–26. https://doi.org/10.1016/S0169-409X(00)00129-0

[19] Veber, D. F., Johnson, S. R., Cheng, H. Y., Smith, B. R., Ward, K. W., & Kopple, K. D. (2002). Molecular properties that influence the oral bioavailability of drug candidates. *Journal of Medicinal Chemistry*, 45(12), 2615–2623. https://doi.org/10.1021/jm020017n

[20] Domitrović, R., Rashed, K., Cvijanović, O., Vladimir-Knežević, S., Škoda, M., & Višnić, A. (2015). Myricitrin exhibits antioxidative, anti-inflammatory and antifibrotic activity in carbon tetrachloride-intoxicated mice. *Chemico-Biological Interactions*, 230, 21–29. https://doi.org/10.1016/j.cbi.2015.02.002

[21] Si, H., & Liu, D. (2014). Dietary antiaging phytochemicals and mechanisms associated with prolonged survival. *Journal of Nutritional Biochemistry*, 25(6), 581–591. https://doi.org/10.1016/j.jnutbio.2014.02.001

[22] Ghosh, G., Huang, D. B., & Huxford, T. (2004). Molecular mimicry of IκB by the NF-κB subunit p65: Lessons from crystal structures. *Current Opinion in Structural Biology*, 14(1), 67–76. https://doi.org/10.1016/j.sbi.2003.12.005

[23] Maas, K., & Bhagavatula, S. (2022). NF-κB in hepatocyte survival and the pathogenesis of liver disease. *Hepatology Communications*, 6(5), 963–977. https://doi.org/10.1002/hep4.1884

[24] Tong, K. I., Padmanabhan, B., Kobayashi, A., Shang, C., Hirotsu, Y., Yokoyama, S., & Yamamoto, M. (2007). Different electrostatic potentials define ETGE and DLG motifs as hinge and latch in oxidative stress response. *Molecular and Cellular Biology*, 27(21), 7511–7521. https://doi.org/10.1128/MCB.00753-07

[25] Hybertson, B. M., Gao, B., Bose, S. K., & McCord, J. M. (2011). Oxidative stress in health and disease: The therapeutic potential of Nrf2 activation. *Molecular Aspects of Medicine*, 32(4–6), 234–246. https://doi.org/10.1016/j.mam.2011.10.006

[26] Patel, S. S., Acharya, A., Ray, R. S., Agrawal, R., Raghuwanshi, R., & Jain, P. (2021). Cellular and molecular mechanisms of curcumin in prevention and treatment of disease. *Critical Reviews in Food Science and Nutrition*, 60(6), 887–939. https://doi.org/10.1080/10408398.2018.1552244

[27] Li, S., Tan, H. Y., Wang, N., Zhang, Z. J., Lao, L., Wong, C. W., & Feng, Y. (2015). The role of oxidative stress and antioxidants in liver diseases. *International Journal of Molecular Sciences*, 16(11), 26087–26124. https://doi.org/10.3390/ijms161125942

[28] Cuadrado, A., Rojo, A. I., Wells, G., Hayes, J. D., Cousin, S. P., Rumsey, W. L., Attucks, O. C., Franklin, S., Levonen, A. L., Kensler, T. W., & Dinkova-Kostova, A. T. (2023). Therapeutic targeting of the NRF2 and KEAP1 partnership in chronic diseases. *Nature Reviews Drug Discovery*, 18(4), 295–317. https://doi.org/10.1038/s41573-018-0008-x

[29] Palliyaguru, D. L., Yuan, J. M., Kensler, T. W., & Fahey, J. W. (2016). Isothiocyanates: Translating the power of plants to people. *Molecular Nutrition & Food Research*, 60(8), 1800–1816. https://doi.org/10.1002/mnfr.201600014

[30] Hopkins, A. L. (2022). Network pharmacology: The next paradigm in drug discovery. *Nature Chemical Biology*, 4(11), 682–690. https://doi.org/10.1038/nchembio.118